Mechanics of Materials 140 (2020) 103211

Contents lists available at ScienceDirect

Mechanics of Materials

journal homepage: www.elsevier.com/locate/mechmat

Research paper

Numerical investigation of the temperature dependence of dynamic yield stress of typical BCC metals under shock loading with a dislocation-based constitutive model

Songlin Yao[a], Xiaoyang Pei[a], Zhanli Liu[b], Jidong Yu[a,*], Yuying Yu[a], Qiang Wu[a]

[a] National Key Laboratory of Shock Wave and Detonation Physics, Institute of Fluid Physics, China Academy of Engineering Physics, Mianyang, Sichuan 621900, China
[b] Applied Mechanics Laboratory, School of Aerospace Engineering, Tsinghua University, Beijing 100084, China

ARTICLE INFO

Keywords:
Dislocation substructure
Shock loading
Dynamic yield stress
Temperature effect

ABSTRACT

Interpretation of the temperature dependence of the dynamic yield stress of shock-loaded metals has recently become a critical problem in shock wave physics. However, the temperature dependence of the dynamic yield stress of BCC metals is rarely investigated owing to the lack of an accurate description of the constitutive behavior of BCC metals subjected to high strain rate and high temperature. To unravel the underlying mechanism of the dynamic yield stress of BCC metals under such extreme conditions, we established a dislocation-based constitutive model in which the dislocation generation equation is proposed from the viewpoint of dissipation energy. When applied to shock-loaded BCC metals, this model reproduced the elastic–plastic wave characteristics observed in preheated plate-impact experiments quantitatively even at temperatures of >1000 K. It was found that forest hardening induced by thermally activated homogeneous nucleation (TA-HN) serves as the primary contributing factor to the thermal hardening behavior of vanadium at elevated temperature, while Peierls stress serves as the primary contributing factor to the thermal softening behaviors of other BCC metals. The novelty of this work lies in that the forest hardening mechanism, as a plastic hardening mechanism and usually regarded as temperature insensitive for BCC metals, has been proved to be temperature sensitive and influence dislocation motion significantly owing to TA-HN at high strain rate and high temperature. Based on this mechanism, we also predicted that the thermal hardening behavior would also occur in other BCC metals, e.g., molybdenum and tungsten, at temperature ranges beyond the limit of existing experiments.

1. Introduction

Study of the dynamic deformation of metals under shock wave loading is critical to many technical applications, e.g., high-speed impact phenomena, vehicular crash tests, and development of armor. Owing to the strain rate dependence of the deformation mechanisms, dynamic strength behavior at shock wave loading differs significantly from that at quasi-static states or moderate strain rates. In recent years, numerous works (Luscher et al., 2013; Lloyd et al., 2014; De et al., 2014) have addressed the constitutive behaviors of metals at shock wave loading. Nonetheless, the physical principle of dynamic strength under such extreme conditions is still not well understood. It has been found that dynamic strength is influenced by numerous external factors, including applied stress (Meyers et al., 2009), strain rate, and temperature (Kanel et al., 2014). Among these factors, temperature has long been regarded as a critical factor to the strength of metals (Cui et al., 2016) and has recently become a popular topic in the study of the dynamic strength of metals (Krasnikov et al., 2011; Mayer et al. 2013; Kanel 2014; Gurrutxaga-Lerma et al., 2017).

In early studies (Lennon and Ramesh, 2004; Voyiadjis and Abed, 2005), focus was placed on the strength of a metal at moderate strain rate and in a quasi-static state, and it was found that the strength of a metal decreases significantly with increasing temperature. A widely accepted interpretation of this phenomenon is that the plastic deformation is governed by the thermal activation mechanism at this strain rate range. The fundamental origin of the thermal activation mechanism lies in a dislocation overcoming the Peierls barrier to move with the aid of thermal fluctuation when the external applied stress is not high enough (Kuskin and Yanilkin, 2013). Based on this theory, constitutive models could describe the plastic response of metals at moderate strain rates, $<10^4$ s^{-1}, effectively, and predicted a thermal softening behavior of the strength.

* Corresponding author.
E-mail address: yujidong@caep.cn (J. Yu).

https://doi.org/10.1016/j.mechmat.2019.103211
Received 2 May 2019; Received in revised form 12 October 2019; Accepted 13 October 2019
Available online 20 October 2019

Recently, Kanel and Zaretsky found that the temperature dependence of the dynamic yield stress of shock-loaded metals, where strain rate can be $>10^4\ s^{-1}$, differs considerably from that at moderate strain rate, $<10^4\ s^{-1}$ (Kanel, 2014). In particular, the thermal hardening behavior of the dynamic yield stress of shock-loaded metals opposes the thermal softening behavior of those under a quasi-static state or a moderate strain rate. Thermal hardening behavior is observed in most FCC and HCP metals. However, most BCC metals still exhibit thermal softening behaviors (Zaretsky and Kanel, 2014, 2016, 2017) at the same strain rate range except for iron (Zaretsky, 2009) and vanadium (Zaretsky and Kanel, 2014). In particular, the HEL spikes of vanadium are temperature insensitive, whereas the HEL minima exhibit a distinct increase as temperature increases from 800 K to 1100 K. Here, we define this behavior as thermal hardening of the dynamic yield stress. Besides that, twinning was also observed in the recovered vanadium sample. For iron, the dynamic yield strength exhibits an anomalous thermal hardening behavior around the Curie temperature.

Constitutive models, based on thermally activated dislocation motion, seem incapable of describing dynamically the plastic response of shock-loaded metals, especially the temperature dependence of the dynamic yield stress. From the viewpoint of dislocation motion, a dislocation subjected to a high strain rate could overcome the Peierls barrier easily without the aid of thermal fluctuations because the applied stress at a high strain rate is usually relatively high. For a gliding dislocation, phonon drag and relativistic effects control its motion at relatively low dislocation velocity and at higher dislocation velocity, approaching the transverse sound speed, respectively. Based on this picture, the thermal hardening behavior of FCC metals is attributed to the phonon drag mechanism (Krasnikov et al., 2011; Mayer et al., 2013) and the shear modulus (Gurrutxaga-Lerma et al., 2017). Nonetheless, it seems that these two thermal hardening mechanisms are not suitable for shock-loaded BCC metals because of the relatively high Peierls stress of BCC metals. When addressing the temperature dependence of the dynamic strength of shock-loaded iron, Gurrutxaga-Lerma highlighted the role of Peierls stress on dislocation motion and pointed out that the increasing phonon drag hardening is counterbalanced by the rapid drop of Peierls stress. Apart from that, the relativistic effect is difficult to achieve because of relatively high resistance for a gliding dislocation in a BCC metal. Moreover, the anomalous temperature-dependent behavior of the shear modulus of vanadium at >800 K (Walker, 1978) invalidates the relativistic effect, although the dislocation velocity approaches the transverse sound speed.

As opposed to dislocation motion, dislocation generation has also been proposed as the main contributing factor to strength as strain rate increases. In particular, homogeneous nucleation has long been proposed as a likely mechanism for the generation of dislocations at shock fronts. Armstrong et al. (2009) pointed out that a transition from thermally activated dislocation motion at moderate strain rate to thermally activated dislocation generation at very high strain rate is responsible for the upturn behavior of the strength around a strain rate of $10^4\ s^{-1}$. Obviously, a constitutive model based on thermally activated dislocation generation also predicts a thermal softening behavior, like a constitutive model based on thermally activated dislocation motion does, but is still incapable of explaining the thermal hardening behaviors at high strain rates.

Besides dislocations, deformation twinning is also a shear deformation mechanism, especially in BCC and HCP metals. Atomistic simulation indicates that there exists a transition from dislocation motion to twinning as shear stress exceeds the threshold stress for twinning. It is found that twinning can more easily occur at low temperature because Peierls stress for perfect dislocations increases more rapidly as temperature decreases than that for partial dislocations. To the authors' knowledge, the effect of twinning deformation on the temperature dependence of the dynamic strength under shock loading has never been discussed before.

Although the shock-loading response of shock-loaded BCC metals has been addressed in several works (Barton et al., 2011; Hansen, 2013; Gurrutxaga-Lerma et al., 2017), it seems that the dynamic plastic deformation of BCC metals has not been described accurately because the plastic deformation mechanisms, including homogeneous nucleation (HN) and twinning, are not considered comprehensively. Moreover, existing models have never been proven to remain effective for BCC metals under high strain rate and elevated temperature (>1000 K).

In this article, a dislocation-based crystal plasticity model is established with the aim at unraveling the underlying temperature dependence mechanism of the dynamic strength of shock-loaded BCC metals. To describe the mechanical response of BCC metals correctly, the controlling mechanisms of dislocation motion, dislocation generation, dislocation annihilation, and twinning shear deformation are comprehensively considered in this model. The innovative feature of this model lies in the dislocation generation equation being proposed from the viewpoint of energy. Different from existing works, the dislocation generation equation in this article is coupled with the shear modulus and is classified as an HN term and a multiplication term. In particular, the HN term is not just the classical Arrhenius equation multiplied by a constant parameter; rather it is multiplied by a thermal-energy-related term. Compared to the classical Arrhenius equation, in this equation, the HN is not only controlled by the applied stress but also by thermal energy. Moreover, this model also couples dislocation evolution with twinning, making it possible to study the competition between twinning and dislocation evolution during dynamic yielding. Using this model, we simulated the shock-loading response of typical BCC metals, including tantalum, vanadium, molybdenum, tungsten, and iron. The simulated velocity profiles match well with experimental results, including elastic–plastic wave characteristics and the temperature dependence of the dynamic yield stress.

2. Thermoelastic–viscoplastic model

Under high strain rate and high temperature, the mechanical response of a deformed crystalline metal can be described by a thermoelastic–viscoplastic model, which will be detailed in the following.

The deformation gradient is used to describe the deformation process, $\boldsymbol{F} = \frac{d\boldsymbol{y}}{d\boldsymbol{x}}$. For a thermoelastic–viscoplastic system, the deformation gradient can be decomposed into three components (De et al., 2014):

$$\boldsymbol{F} = \boldsymbol{F^e F^t F^p}, \tag{1}$$

where $\boldsymbol{F^e}$, $\boldsymbol{F^t}$, and $\boldsymbol{F^p}$ denote the elastic deformation gradient, thermal deformation gradient, and plastic deformation gradient, respectively. The spatial gradient of total velocity, defined as $\boldsymbol{L} = \dot{\boldsymbol{F}}\boldsymbol{F}^{-1}$, can be expressed by the following additive decomposition:

$$\boldsymbol{L} = \dot{\boldsymbol{F}}^{\boldsymbol{e}}\boldsymbol{F}^{e-1} + \boldsymbol{F}^{\boldsymbol{e}}\dot{\boldsymbol{F}}^{\boldsymbol{t}}\boldsymbol{F}^{t-1}\boldsymbol{F}^{e-1} + \boldsymbol{F}^{\boldsymbol{e}}\boldsymbol{F}^{\boldsymbol{t}}\dot{\boldsymbol{F}}^{\boldsymbol{p}}\boldsymbol{F}^{p-1}\boldsymbol{F}^{t-1}\boldsymbol{F}^{e-1}. \tag{2}$$

The spatial velocity gradient of the plastic shear deformation (Roters et al., 2010) and thermal deformation can be expressed as

$$\dot{\boldsymbol{L}}^{\boldsymbol{p}} = \dot{\boldsymbol{F}}^{\boldsymbol{p}}\boldsymbol{F}^{p-1} = \left(1 - \sum_{\beta=1}^{N_{tw}} \gamma_{tw}^{\beta}\right) \sum_{\alpha=1}^{N_{dis}} \dot{\gamma}_{dis}^{\alpha} \boldsymbol{s}_0^{\alpha} \otimes \boldsymbol{m}_0^{\alpha} + \sum_{\beta=1}^{N_{tw}} \dot{\gamma}_{tw}^{\beta} \boldsymbol{s}_{\boldsymbol{tw}}^{\beta} \otimes \boldsymbol{m}_{\boldsymbol{tw}}^{\beta} + \sum_{\beta=1}^{N_{tw}} \gamma_{tw}^{\beta} \sum_{\alpha=1}^{N_{dis}} \dot{\gamma}_{dis}^{\alpha} \boldsymbol{Q}\boldsymbol{s}_0^{\alpha} \otimes \boldsymbol{m}_0^{\alpha}\boldsymbol{Q}^{\boldsymbol{T}}, \tag{3}$$

$$\dot{\boldsymbol{L}}^{\boldsymbol{t}} = \dot{\boldsymbol{F}}^{\boldsymbol{t}}\boldsymbol{F}^{t-1} = \dot{T}\boldsymbol{\zeta}, \tag{4}$$

where $\dot{\gamma}_{dis}^{\alpha}$ is the plastic shear rate in slip system α with slip direction $\boldsymbol{s}_0^{\alpha}$ and slip plane normal $\boldsymbol{m}_0^{\alpha}$ in the reference configuration, N_{dis} is the number of slip systems, N_{tw} is the number of twinning systems, $\dot{\gamma}_{tw}^{\beta}$ is the plastic shear rate in twinning system β with twinning direction $\boldsymbol{s}_{\boldsymbol{tw}}^{\beta}$ and plane normal $\boldsymbol{m}_{\boldsymbol{tw}}^{\beta}$ in the reference configuration, matrix $\boldsymbol{Q}$ is used to reorient the single crystalline parent volume owing to the activation of twinning, $\boldsymbol{\zeta}$ is the thermal expansion tensor and treated as isotropic for BCC symmetry, and $\dot{T}$ is the temperature change rate during the deformation. Because the fraction of twinning in the deformation

addressed in this work is small, the third term in Eq. (3) is ignored.

2.1. Thermoelastic formation

We now derive the stress tensor expression from the internal energy of a deformed system. The internal energy of a thermo-elastic–viscoplastic system can be written as (Lloyd et al., 2014)

$$\mathcal{E} = \mathcal{E}(\varepsilon^e, \eta, \xi), \tag{5}$$

where ε^e is a reference elastic strain measure, η is the entropy, and ξ is an internal state variable that quantifies the lattice defect contribution to the total energy. Expanding the internal energy about a reference state up to second order in elastic strain and first order in entropy change gives

$$\mathcal{E} = \mathcal{E}_0 + \varepsilon^e : \left(\frac{\partial \varepsilon}{\partial \varepsilon^e}\right)_{\varepsilon^e=0} + \frac{1}{2}\varepsilon^e : \left(\frac{\partial^2 \varepsilon}{\partial \varepsilon^e \partial \varepsilon^e}\right)_{\varepsilon^e=0} : \varepsilon^e + T\Delta\eta + f(\xi). \tag{6}$$

Apparently, higher order elastic strain should be considered to describe the mechanical response at finite deformation more accurately and rigorously. However, to a good approximation, especially for elastic–plastic materials, third and higher order elastic constants are usually ignored (De et al., 2014).

Following the thermoplastic model derived by De et al. (2014), the stress tensor equation can be obtained from the stress-dependent and entropy-dependent internal energy. By taking into account the pressure and temperature dependence of the elastic constant tensor, which are significant for high loading rates (De et al., 2014), the work conjugate stress of the strain can be defined as

$$\boldsymbol{\sigma} = \mathbb{C} : \boldsymbol{\varepsilon}^e + \frac{1}{2}\left[\boldsymbol{\varepsilon}^e : \frac{\partial \mathbb{C}}{\partial P} : \boldsymbol{\varepsilon}^e\right]\frac{\partial P}{\partial \varepsilon_V^e}\boldsymbol{I} + \frac{1}{2}\left[\boldsymbol{\varepsilon}^e : \frac{\partial \mathbb{C}}{\partial T} : \boldsymbol{\varepsilon}^e\right]\frac{\partial T}{\partial \varepsilon^e} + \frac{\partial T}{\partial \varepsilon^e}\Delta\eta, \tag{7}$$

where $\mathbb{C} = (\frac{\partial^2 \varepsilon}{\partial \varepsilon^e \partial \varepsilon^e})_{\varepsilon^e=0}$ is the second-order elastic constant, ε_V^e is the volumetric component of the elastic strain tensor, and P is the pressure. By following Maxwell's thermomechanical relation,

$$\frac{\partial T}{\partial \boldsymbol{\varepsilon}^e} = \frac{\partial^2 \varepsilon}{\partial \boldsymbol{\varepsilon}^e \partial \eta} = -T\boldsymbol{\Gamma}, \tag{8}$$

the stress can be expressed as

$$\boldsymbol{\sigma} = \mathbb{C} : \boldsymbol{\varepsilon}^e + \frac{1}{2}\left[\boldsymbol{\varepsilon}^e : \frac{\partial \mathbb{C}}{\partial P} : \boldsymbol{\varepsilon}^e\right]\frac{\partial P}{\partial \varepsilon_V^e}\boldsymbol{I} - \frac{1}{2}\left[\boldsymbol{\varepsilon}^e : \frac{\partial \mathbb{C}}{\partial T} : \boldsymbol{\varepsilon}^e\right]T\Gamma\boldsymbol{I} - T\Gamma\boldsymbol{I}\Delta\eta, \tag{9}$$

where $\boldsymbol{\Gamma}$ is the Grüneisen tensor.

For shock-loading problems, the mechanical response is usually decomposed into a spherical part and a deviatoric part, and the spherical part is mainly described by an equation of state (EOS). Here, the stress tensor is split into hydrostatic σ_h and deviatoric σ' components:

$$\sigma_h = \sigma_{EOS} + \frac{1}{3}\left(\boldsymbol{\varepsilon}'^e : \mathbb{C} : \boldsymbol{I}\right) + \left[\frac{1}{2}\left(\boldsymbol{\varepsilon}'^e : \frac{\partial \mathbb{C}}{\partial P} : \boldsymbol{\varepsilon}'^e\right) + \frac{1}{3}\left(\boldsymbol{\varepsilon}'^e : \frac{\partial \mathbb{C}}{\partial P} : \boldsymbol{I}\varepsilon_V^e\right)\right]\frac{\partial P}{\partial \varepsilon_V^e} - \frac{1}{2}\left[\boldsymbol{\varepsilon}^e : \frac{\partial \mathbb{C}}{\partial T} : \boldsymbol{\varepsilon}^e\right]T\Gamma - T\Gamma\Delta\eta, \tag{10a}$$

and

$$\sigma' = \ell : \mathbb{C} : \boldsymbol{\varepsilon}^e, \tag{10b}$$

where $\boldsymbol{\varepsilon}'^e$ is the deviatoric part of the strain tensor and ℓ represents a fourth-order operator that extracts the deviatoric part from a second-order tensor. σ_{EOS} is used to represent the terms that are purely related to volume change, i.e.,

$$\sigma_{EOS} = \frac{1}{9}(\boldsymbol{I} : \mathbb{C} : \boldsymbol{I})\varepsilon_V^e + \frac{1}{18}(\varepsilon_V^e)^2\left(\boldsymbol{I} : \frac{\partial \mathbb{C}}{\partial P} : \boldsymbol{I}\right)\frac{\partial P}{\partial \varepsilon_V^e}. \tag{11}$$

In this work, the EOS term is replaced by the Grüneisen EOS (Abaqus Analysis User's Guide, 2016),

$$\sigma_{EOS} = \frac{\rho_0 C_0^2 \mu}{(1 - s\mu)^2}, \tag{12}$$

where C_0 and s are critical parameters determined by experiments, and $\mu = 1 - \rho_0/\rho$ is the nominal volumetric compressive strain. Obviously, the EOS term can be replaced by other EOS models, such as the Birch–Murnaghan model (Lloyd et al., 2014).

The rates at which temperature and entropy change are expressed as

$$T\dot{\eta} = -\mathrm{div}\boldsymbol{q} + \sigma^L : \dot{\varepsilon}^p, \tag{13}$$

$$C_V \dot{T} = -\mathrm{div}\boldsymbol{q} + C_V T\boldsymbol{\Gamma} : \dot{\varepsilon}^e + \sigma^L : \dot{\varepsilon}^p, \tag{14}$$

where $\boldsymbol{q}$ denotes the heat flux. The heat transmission term can be ignored because deformation induced by shock loading is so quick that heat transmission is not significant. Then rates at which temperature and entropy change can be expressed as (De et al., 2014)

$$T\dot{\eta} = \sigma^L : \dot{\boldsymbol{\varepsilon}}^p, \tag{15}$$

$$\mathrm{C}_V \dot{T} = \mathrm{C}_V T\boldsymbol{\Gamma} : \dot{\boldsymbol{\varepsilon}}^e + \sigma^L : \dot{\boldsymbol{\varepsilon}}^p. \tag{16}$$

2.2. Single-crystal plasticity kinetics

In this article, plastic deformation is attributed to dislocations and twinning. Dislocation motion and dislocation generation together control the plastic deformation plastic strain rate according to the generalized Orowan equation

$$\dot{\gamma}_{dis}^{\alpha} = b\rho_M^{\alpha} V_D^{\alpha} + (\dot{\rho}_M^{\alpha} + \dot{\rho}_{IM}^{\alpha})b\bar{l}, \tag{17}$$

where ρ_M, $\dot{\rho}_M$, $\dot{\rho}_{IM}$, V_D, and $\bar{l}$ refer to mobile dislocation density, generation rate of mobile dislocations, generation rate of immobile dislocations, dislocation velocity, and the displacement a dislocation segment undergoes during its formation, respectively. Thus plastic deformation is determined by dislocation motion, dislocation generation, and twinning deformation, which will be depicted in detail in the following.

Dislocations can have either edge character or screw character. For BCC metals, the mobility of the edge dislocations is much higher than that of the screw dislocations, which leads to that the area encountered by the edge dislocations during the plastic slip is much smaller than that encountered by the screw dislocations (Cui et al., 2016). The area encountered by the dislocation line during dislocation motion represents the plastic deformation. Therefore, the edge dislocations play a minor role on the plastic deformation of BCC metals than the screw dislocations. Barton et al. (2011) has also pointed out that dislocations densities for screw dislocations occupies roughly 60% of the overall population based on dislocation dynamics simulation. In this article, to an approximation, we did not distinguish dislocation characters, and we mainly took screw dislocations into account, like Barton et al. (2011) did.

2.2.1. Dislocation motion

A dislocation will not glide until applied stress exceeds the mechanical threshold stress, also known as the critical resolved shear stress (CRSS), which mainly includes the Peierls stress τ_p, dislocation–dislocation interaction resistance τ_{int}, and athermal resistance τ_a. The non-Schmid effect is not considered in this study because the Schmid effect is not significant at the temperature range addressed here (Chen et al., 2013). The mechanical threshold stress may be written as

$$\tau_c = \tau_p + \tau_{int} + \tau_a. \tag{18}$$

Peierls stress is usually regarded as the main resistance in a BCC metal, and it drops with temperature considerably. The temperature dependence of Peierls stress, based on the theory proposed by Smirnov (1967), can be expressed as

$$\tau_p(T)/\tau_{p0} = \exp\left\{-\frac{36qh^2N_A}{2\pi k_B b^2 A_m \Theta_D}\left[\frac{D_3(x)}{x}\right]\right\}, \tag{19}$$

where x denotes Θ_D/T, $D_3(x)$ is a third-order Debye function, $q = G/\tau_T$ denotes the relation between shear modulus G and the ideal shear strength τ_T, τ_{p0} is the Peierls stress at 0 K, h is the Planck's constant, N_A is Avogadro's number, and A_m is atomic weight.

The interaction resistance is often known as 'forest' dislocation work hardening, which indicates that dislocation–dislocation interaction also serves as the obstacle for a dislocation to move (Madec and Kubin, 2017). The interaction resistance is expressed by a Taylor relation, $\tau_{int} = A_I Gb\sqrt{\rho_{IM}}$, in which A_I is the hardening coefficient, G is the shear modulus, and ρ_{IM} is immobile dislocation density.

The long-range resistance serves as an athermal threshold below which there is no viscoplastic flow. As detailed in the multiscale strength model (Barton et al., 2011), this athermal resistance could be connected notionally to grain structure and does not contribute significantly to the strength results.

Below the mechanical threshold stress, a dislocation cannot move without the aid of thermal fluctuation. Based on this picture, thermally activated dislocation motion is usually proposed to describe the dislocation evolution at moderate strain rate. Given that the applied stress in shock loading is usually much higher than the mechanical threshold stress, which makes thermally activated dislocation motion impossible, we did not take the thermally activated dislocation motion mechanism into account in this study. Above the mechanical threshold stress, a dislocation will move along the slip system, which is ⟨111⟩{110}for BCC metals. During its motion, a dislocation has to overcome phonon drag resistance. Apart from phonon drag viscosity, a gliding dislocation in a BCC metal will also overcome the viscosity caused by self-pinning and unpinning (Marian et al., 2004). Therefore, we introduced the effective viscosity, summation of phonon drag viscosity, and pinning–unpinning viscosity to control the dislocation motion above the mechanical threshold stress. The effect of temperature on the effective viscosity is attributed to phonon drag. The phonon drag coefficient is based on the theoretical deduction by Kuskin and Yanilkin (2013) and is given by

$$B_{ph} = 8\pi^2\Gamma^2\frac{h}{b^3}\left(\frac{k_D b}{2\pi}\right)^5\left[\frac{D_3(x)}{x}\right], \tag{20}$$

where Γ is the Grüneisen coefficient and k_D is the Debye wave vector. The viscosity caused by self-pinning and unpinning is taken as an adjustable parameter and assumed to be temperature independent. Therefore, the dislocation velocity governing equation can be written as (Hirth et al., 1998)

$$\frac{d}{dt}\left(\frac{m_0 V_D}{\sqrt{1 - V_D^2/c_t^2}}\right) = (\tau - \tau_c)b - \frac{(B_{pin} + B_{ph})V_D}{\sqrt{1 - V_D^2/c_t^2}}, \tag{21}$$

where m_0 is the dislocation mass, c_t is the transverse sound speed, τ is the resolved shear stress, and B_{pin} is defined as the effective viscosity caused by self-pinning and unpinning and is taken as temperature insensitive and adjustable.

2.2.2. Dislocation substructure evolution

When the shock wave arrives, the sharp rise of the shear stress serves as the driving force for dislocation generation and motion. The mobile segments glide on the slip plane until they are annihilated or immobilized by obstacles. Based on this conceptualization of dislocation evolution, dislocations can be classified as mobile dislocations and immobile dislocations, and the dislocation density equations, as written by Austin and McDowell (2012), are

$$\dot{\rho}_M = \chi\dot{\rho}_{HN} + \dot{\rho}_{mult} - \dot{\rho}^M_{anni} - \dot{\rho}_{trap}, \tag{22a}$$

$$\dot{\rho}_{IM} = (1 - \chi)\dot{\rho}_{HN} + \dot{\rho}_{trap} - \dot{\rho}^{IM}_{anni}, \tag{22b}$$

in which terms with subscripts *HN, mult, anni*, and *trap* refer to HN, multiplication, annihilation, and trapping respectively. χ is the fraction of homogeneously nucleated dislocations that remain mobile after traveling a distance $\bar{\chi}_{hom}$ (Austin and McDowell, 2012). Besides homogeneous nucleation, heterogeneous nucleation also contributes to plastic deformation, especially for polycrystalline metals. Nonetheless, for simplicity, heterogeneous nucleation is not taken into account because we are dedicated to addressing the effect of temperature on the dynamic yield stress, and thermally activated HN (TA-HN) is more sensitive to temperature than heterogeneous nucleation. The substructure evolution is explained in the following.

Multiplication: Dislocation line length may be generated by the multiplication of preexisting dislocation segments. At low strain rates, Frank–Read sources and cross-slip are regarded as common dislocation multiplication mechanisms. A widely used multiplication generation equation is the form derived by Johnston and Gilman (1960), which suggests that the multiplication rate is proportional to the plastic strain rate. However, it seems that Johnston and Gilman's equation has not captured the essence of the multiplication process because there exists a constant parameter with a dimension of dislocation density in the equation. In this article, we modified the energy-based multiplication generation equation derived by Krasnikov et al. (2011). It is assumed that the energy of plastic dissipation provides the energy for newly generated dislocations. The dislocation multiplication generation rate is thus proportional to the plastic dissipation rate: $\dot{\rho}_{mult} = A\frac{\dot{\varepsilon}_{dissp}}{W_s}$, where A is a multiplication coefficient, $\dot{\varepsilon}_{dissp} = \tau\dot{\gamma}_p$ is the plastic dissipation rate, and $W_s = \frac{Gb^2}{4\pi}\ln\frac{R}{r_0}$ is the elastic energy per unit length of screw dislocation, with R being the radial distance to the dislocation line and r_0 being the cutoff radius of the dislocation core (Hirth and Lothe, 1968). Thus, the dislocation multiplication equation can be written as

$$\dot{\rho}_{mult} = \alpha_{mult}\frac{\tau\dot{\gamma}_p}{Gb^2}, \tag{23}$$

where α_{mult} is a dimensionless parameter.

Homogeneous nucleation: At high strain rates, the activation of dislocation multiplication is expected to be insufficient to produce enough dislocations during the rise time of the shock front. Thus, HN generation, a fast-acting mechanism, becomes more fundamental. Usually, the HN generation rate is of a classical Arrhenius form, which describes the probabilistic nature of thermal activation. In this article, the HN generation equation is expressed as an Arrhenius equation multiplied by a term associated with thermal energy. In contrast from the viewpoint of energy of plastic dissipation, thermal energy is regarded as responsible for the thermally activated dislocation nucleation because HN is thermally activated when applied stress is below the nucleation stress. The HN generation equation is expressed as

$$\dot{\rho}_{HN} = \alpha_{HN}\frac{k_B T}{Gb^3}\exp\left(-\frac{Q_0 - \tau\Omega}{k_B T}\right), \tag{24}$$

where k_BT is the thermal energy, Ω is the activation volume and set as b^3, and Gb^3 is proportional to the elastic energy per b of dislocation. It is suggested by this model that the dislocation generation rate is inversely proportional to the shear modulus.

Annihilation: Dislocation annihilation occurs when two dislocation with opposite signs are close. For mobile dislocations, dislocation annihilation includes annihilation induced by interaction between mobile dislocations and annihilation induced by interaction between mobile dislocations and immobile dislocations. For immobile dislocations, the annihilation process is all attributed to annihilation induced by interaction between mobile dislocations and immobile dislocations. Hence, the annihilation equation is written as (Mayer et al., 2013)

$$\dot{\rho}^M_{anni} = \alpha_{anni}\rho_M V_D b(\rho_M + \rho_{IM}), \tag{25a}$$

$$\dot{\rho}^{IM}_{anni} = \alpha_{anni}\rho_M V_D b\rho_{IM}, \tag{25b}$$

where α_{anni} is the annihilation rate.

Immobilization: When gliding dislocations encounter obstacles, part of the gliding dislocations may be immobilized. Immobilized dislocations are transferred as an immobile dislocation population. We adopt the equation derived by Mayer et al. (2013) to describe this process. The immobilization speed is proportional to the mobile dislocation density and negatively proportional to a characteristic time:

$$\dot{\rho}_{trap} = V_I(\rho_M - \rho_0)\sqrt{\rho_{IM}}, \tag{26}$$

where V_I is the trapping rate and ρ_0 is the minimum dislocation density.

Saturation dislocation density: Following the multiscale strength model (Barton et al., 2011), saturation dislocation density is also introduced in this model to set up the upper limit of dislocation density at specified plastic strain rate,

$$\rho_{sat} = \rho_{s0}\left(\frac{\dot{\varepsilon}^p}{\dot{\varepsilon}_N} + S_0\right)^n \tag{27}$$

Parameters $\dot{\varepsilon}_N$, S_0, and n, which determine the strain rate dependence of ρ_{sat}, are set as the same as those of vanadium for BCC metals discussed in this article, whereas ρ_{s0} is adjusted properly to discuss the effect of ρ_{sat} on the temperature dependence of the dynamic yield stress at higher temperature.

2.2.3. Deformation twinning

Compared to FCC metals, twinning can more easily occur in BCC metals subjected to shock loading. Marian et al. (2004) pointed out that there exists a transition from dislocation motion to twinning as shear stress increases when the twinning threshold stress is higher than the Peierls stress. Twinning is also a shear deformation mechanism and plays the same role as dislocation does during plastic deformation. Under high applied stress, a twin is nucleated in a grain and then propagates on the twinning plane along the twinning shear direction (Wu et al., 2015). Based on this picture, Wu et al. (2015) proposed a twin nucleation, propagation, and growth model to describe the evolution of twinning in AZ31. In this study, we aim to address the effect of twinning on the mechanical response at elevated temperatures. Under this conditions, the effect of dislocations on the mechanical response is more significant than that of twinning. Consequently, we adopted a phenomenological twinning model and did not distinguish the substructure evolution of twinning to investigate the collective behaviors of twinning. The twinning kinetics follows the power law form

$$\dot{\gamma}_{tw}^{\beta} = \begin{cases} \dot{\gamma}_{tw}^0(\tau^{\beta}/\tau_{tw})^{1/r}, & \tau > \tau_{tw}, \\ 0, & \tau < \tau_{tw}, \end{cases} \tag{28}$$

where τ_{tw} is the twinning threshold stress below which twins do not form, τ is the resolved shear stress, β denotes the twinning system, which is set as ⟨112⟩{110} for BCC vanadium, $\dot{\gamma}_{tw}^0$ is the reference twinning rate, and r is the rate-sensitivity power coefficient (Florando et al., 2013).

2.2.4. Polycrystal model

The above theory is applied to describe the mechanical response of monocrystalline material. To describe the mechanical response of polycrystalline materials, a simplified polycrystal model is established. For high-symmetry polycrystalline materials, the assumption that the local deformation gradient in each grain is homogeneous and identical to the macroscopic deformation gradient at the continuum material point level is adopted. In this case, we ignored the effect of grain boundary and only considered the distribution of the orientation of grains along the loading direction. The number of grains is determined by the sample size along the loading direction divided by real grain size, ~30 μm. Ignoring the effect of the grain boundary is acceptable because the effect of the grain boundary on the width of the wave front has been proved to be small compared to grain-to-grain anisotropy by atomistic simulations (Bringa et al. 2005). The polycrystal model is displayed in Fig. 1.

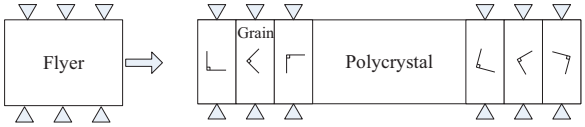

Fig. 1. Schematic of a plate-impact experiment and polycrystal model.

With $\sigma^{(k)}$ denoting the constant Cauchy stress in each grain, the volume-average Cauchy stress is given as

$$\bar{\sigma} = \sum_{k=1}^{N} V^{(k)}\sigma^{(k)}, \tag{29}$$

where $V^{(k)}$ is the volume fraction of each grain. Because all the grains are assumed to be of the same volume, the stress is just the average over all the grains,

$$\bar{\sigma} = \frac{1}{N}\sum_{k=1}^{N} \sigma^{(k)}, \tag{30}$$

where N denotes the grain number along the loading direction.

2.3. Determination of parameters

2.3.1. Material parameters

Initial elastic constants at different temperatures are determined by the temperature dependence of the elastic constants,

$$c_{ij} = c_{ij}^0 + \frac{\partial c_{ij}}{\partial T} \times (T - T_0) + \frac{\partial^2 c_{ij}}{\partial T^2} \times (T - T_0)^2, \tag{31}$$

where c_{ij} represents $\mathbb{C}_{mnkl}$ with m denotes ij and n denotes kl, $\frac{\partial c_{ij}}{\partial T}$ is the temperature derivative of c_{ij}, and $\frac{\partial^2 c_{ij}}{\partial T^2}$ is the second order temperature derivative of c_{ij}. Particularly, the second-order temperature derivative is used to describe the anomalous temperature dependence of c_{44} of vanadium and tantalum below ~1000 K (Walker, 1978; Walker and Bujard, 1980). To describe the mechanical response induced by temperature change during the deformation, temperature derivatives of the elastic constants at a specified temperature are calculated by differentiating Eq. (31) with respect to temperature. The values of the elastic constants are listed in Table 1. The pressure derivatives and the temperature derivatives of the elastic constants are listed in Tables 2 and 3, respectively.

The equivalent shear modulus is calculated by Voigt's expression (Jamal, 2014),

$$G = (c_{11} - c_{12} + 3c_{44})/5. \tag{32}$$

The bulk modulus is calculated by using the equation (Soga, 1966)

$$B = (c_{11} + 2c_{12})/3. \tag{33}$$

The elastic constants of vanadium, tantalum, iron, molybdenum and tungsten are obtained from Greiner, 1979, Walker and Bujard (1980), Adams et al. (2006), Dickinson and Armstrong (1967), and Soga (1966), respectively. Pressure derivatives of the elastic constants of vanadium and tantalum are obtained from Katahara and Manghnani (1976) and Varshi (1970), while those of other three metals are not found in existing literatures yet. Temperature derivatives of elastic constants of five metals are obtained from Walker (1978),

Table 1
Elastic constants (in GPa).

	V	Ta	Fe	Mo	W
c_{11}	244.05	266.5	239.26	480.36	534.71
c_{12}	120.96	161.4	135.78	156.17	209.16
c_{44}	51.08	86.56	120.72	112.17	163.38

Table 2
Pressure derivatives.

	V	Ta	Fe	Mo	W
$\partial c_{11}/\partial p$	3.45	5.1			
$\partial c_{12}/\partial p$	3.09	3.14			
$\partial c_{44}/\partial p$	0.50	0.995			

Walker and Bujard (1980), and Varshi (1970). In particular, the elastic constants for Fe, Mo, and W change with temperature linearly in the temperature range between 300 and 1300 K, while those for Ta and V change nonlinearly in the same temperature range (Walker, 1978; Walker and Bujard, 1980). That is why we considered the second-order temperature dependence of V and Ta but not that of the other three metals.

The EOS parameters are listed in Table 4. ρ_0 is the mass density at room temperature. c_0 and λ are the intercept and the slope of the $u_s - u_p$ curve (Abaqus Analysis User's Guide, 2016'), respectively, where u_s is the shock wave speed and u_p is the particle velocity behind the shock. Γ is the Grüneisen coefficient. The Grüneisen EOS parameters at room temperature are obtained from the Material Properties Library of Autodyn, while those at elevated temperature are obtained from Crichton et al. (2016), Katahara and Manghnani (1976), Molodets (2005), and Kushwah et al., (2003) for vanadium, tantalum, molybdenum, and tungsten, respectively.

The phonon drag coefficients and their temperature derivatives for vanadium, tantalum, iron, and molybdenum are determined by Eq. (12), while those of tungsten are obtained from Po et al. (2016). In particular, the temperature derivative of the phonon drag coefficient of tantalum is set as zero based on calculations performed by Barton et al. (2011). The phonon drag coefficient at a specified temperature T is written as

$$B_{ph}(T) = B_0 + B_T(T - 300). \tag{34}$$

The phonon drag coefficients and their temperature derivatives are listed in Table 5. Some other material parameters, including the Debye temperature, the Peierls stress, the atomic mass, and the Burgers vector, used in the model are listed in Table 6.

2.3.2. Model parameters

Among the 14 model parameters listed in Table 7, four of them (i.e., the multiplication rate α_{mult}, mobile coefficient χ, HN rate α_{HN}, and pinning viscosity coefficient B_{pin}) influence the HEL evolution significantly, while the other parameters are set as constants for all metals. The model parameters are determined as follows:

(1) The multiplication rate α_{mult} and pinning viscosity coefficient B_{pin} are determined by fitting experimental results at room temperature; these are not influenced by TA-HN significantly because of TA-HN's strong temperature sensitivity. Particularly, α_{mult} is estimated based on the viewpoint that ~10% of the dissipated energy serves as the energy for newly generated defects, like Krasnikov et al. (2011) did. B_{pin} is proposed based on the atomistic simulation performed by Marian et al. (2004), in which the effective viscosity of BCC iron is a factor of ~2.5 higher than the phonon drag viscosity alone because of dislocation self-pinning and unpinning. The value of B_{pin} is adjusted within several times of the phonon drag viscosity at room temperature and set as temperature insensitive.

(2) Parameters that control TA-HN, including the HN coefficient α_{HN}, mobile coefficient χ, and average length $\bar{l}$ that a nucleated dislocation segment travels, are determined by fitting experimental results at elevated temperatures. Among these parameters, the role

Table 4
Grüneisen EOS parameters at room temperature.

	V	Ta	Fe	Mo	W
ρ_0 (g/cm^3)	6.1	16.7	7.86	10.2	19.23
c_0 (m/s)	5077.0	3410.0	4610.0	5143.0	1000.0
λ	1.2	1.20	1.73	1.25	1.24
Γ	1.4	1.67	1.67	1.59	1.67

Table 5
Phonon drag viscosity.

Viscosity	V	Ta	Fe	Mo	W
B_0 (10^{-5}Pa s)	9.1	15.7	13.5	7.45	98
B_T (10^{-7}Pa s/K)	4.92		1.0	4.34	8.7

Table 6
Material parameters.

	V	Ta	Fe	Mo	W
Debye temperature Θ_D(K)	380	240	470	450	400
Peierls stress τ_{p0}(MPa)	340	525	900	870	900
Atomic mass A_m(g/mol)	50.94	180.94	55.85	95.94	183.8
Burgers vector b(10^{-10}m)	2.62	2.86	2.25	2.7	2.74

Table 7
Dislocation model parameters.

	V	Ta	Fe	Mo	W
HN coefficient α_{HN}[a] (10^{26} m^{-2} s^{-1})	1	5	0.3	50	80
Multiplication coefficient α_{Mult}[a]	0.08	0.11	0.11	0.11	0.08
Annihilation coefficient α_{anni}[b]	10.0	10.0	10.0	10.0	10.0
Taylor hardening coefficient A_I[a]	0.4	0.4	0.4	0.4	0.4
Immobilization rate V_I[a] (m/s)	1.0	1.0	1.0	1.0	1.0
Initial dislocation density ρ_{min}[b] (10^{11} m^{-2})	5	5	5	5	5
Mobile coefficient χ[a]	0.005	0.005	0.005	0.005	0.005
Average length $\bar{l}$[a]	b	b	b	b	b
Pinning viscosity B_{pin}[a] (10^{-4} Pa s)	6.1	0.73	0.65	6.25	0.0
Athermal resistance τ_a (MPa)[c]	10	10	10	10	10
Saturation dislocation density ρ_{S0}[c] (10^{-12} m^{-2})	4	2	4	4	4
$\dot{\gamma}^{Nc}$[c] (s^{-1})	1	1	1	1	1
S_0[c]	650	650	650	650	650
n[c]	0.56	0.56	0.56	0.56	0.56

[a] Adjusted to fit experimental data.
[b] Obtained from Mayer et al. (2013).
[c] Obtained from Barton et al. (2011).

Table 3
Temperature derivatives.

	V	Ta	Fe	Mo	W
$\partial c_{11}/\partial T$ (GPa/K)	−0.0164	−0.0096	−0.0096	−0.0599	−0.00977
$\partial c_{12}/\partial T$ (GPa/K)	−0.0019	0.0056	0.0056	0.0055	−0.02379
$\partial c_{44}/\partial T$ (GPa/K)	−0.0174	−0.018	−0.018	−0.0106	−0.00161
$\partial^2 c_{11}/\partial T^2$ (GPa/K^2)	-9.6182×10^{-6}	-5.05×10^{-6}	0	0	0
$\partial^2 c_{12}/\partial T^2$ (GPa/K^2)	-3.5620×10^{-6}	-5.05×10^{-6}	0	0	0
$\partial^2 c_{44}/\partial T^2$ (GPa/K^2)	1.6666×10^{-5}	5.05×10^{-6}	0	0	0

of χ should be particularly emphasized. χ is critical to reproduce the thermal hardening phenomenon of the HEL of vanadium. The relatively low value of χ seems to be the result of the quick immobilization process of edge dislocations because of the high mobility of edge dislocations.

(3) In this article, Taylor hardening behavior is regarded as universal for a given crystallographic class of materials, and the Taylor hardening coefficients A_I of all metals are set as 0.4, close to DD simulations (Madec and Kubin, 2017).

(4) Saturation dislocation density is used to address the temperature dependent behavior at higher temperature in case that massively generated dislocations by TA-HN at higher temperature exceeds the up-limit of dislocation density. Parameters to determine the saturation dislocation density are adjusted based on the dislocation dynamics simulations using the multiscale strength model (Barton et al., 2011). During the simulations, to address existing experimental results, the effect of saturation dislocation density is not significant.

2.4. Central difference rule

The proposed model is implemented as a VUMAT into the Abaqus/Explicit finite element code. VUMAT is a user subroutine used to define material behavior. In this study, the VUMAT is used to define the mechanical constitutive behavior of a material. The time integration in Abaqus/Explicit is an explicit central difference scheme (Abaqus Analysis User's Guide, 2016'). In the explicit dynamics analysis (Benson, 1992), the kinematic state u_i is advanced using known values of $\dot{u}_{i-1/2}$ and $\ddot{u}_i$,

$$\dot{u}_{i+1/2} = \dot{u}_{i-1/2} + \frac{\Delta t_{i+1} + \Delta t_i}{2}\ddot{u}_i, \tag{35a}$$

$$u_{i+1} = u_i + \Delta t_{i+1}\dot{u}_{i+1/2}, \tag{35b}$$

where the subscript i refers to the increment number in an explicit dynamics step.

To improve the modeling of high-speed dynamics events, artificial bulk viscosity is introduced in the explicit dynamics analysis. The bulk artificial viscosity is evaluated as (Abaqus Analysis User's Guide, 2016)

$$p_{bv} = \rho(a_2 L\dot{\varepsilon}_{vol})^2 - a_1\rho C_d L\dot{\varepsilon}_{vol}, \quad \text{if } \dot{\varepsilon}_{vol} < 0, \tag{36a}$$

$$p_{bv} = 0, \quad \text{if } \dot{\varepsilon}_{vol} < 0, \tag{36b}$$

where $a_1 = 0.06$ and $a_2 = 1.2$ are the scale factor of the linear and the quadratic viscosity, respectively, $\dot{\varepsilon}_{vol}$ is the volumetric strain rate, L is the element characteristic length, and C_d is the current dilatational wave speed. The discretized form of Eq. (36a) is

$$p_{bv}^{i+1/2} = \rho^{i+1/2}(a_2 L\dot{\varepsilon}_{vol}^{i+1/2})^2 - a_1\rho^{i+1/2}C_d L\dot{\varepsilon}_{vol}^{i+1/2}. \tag{37}$$

Artificial bulk viscosity is implemented into the internal energy equation and the stress tensor:

$$\rho\frac{\partial\varepsilon}{\partial t} = (\sigma_h + p_{bv})\frac{1}{\rho}\frac{\partial\rho}{\partial t} + \boldsymbol{\sigma}' : \dot{\mathbf{e}}, \tag{38}$$

$$\boldsymbol{\sigma} = \boldsymbol{\sigma}' - (\sigma_h + p_{bv})\boldsymbol{I}, \tag{39}$$

where p_{bv} is the bulk artificial viscosity pressure and $\dot{\mathbf{e}}$ is the deviatoric strain rate. The discretized forms of Eqs. (38) and (39) are

$$\rho^{i+1/2}\frac{\varepsilon^{i+1} - \varepsilon^i}{\Delta t_{i+1}} = \frac{1}{2}(\sigma_h^{i+1} + \sigma_h^i + p_{bv}^{i+1} + p_{bv}^i)\frac{1}{\rho^{i+1/2}}\frac{\rho^{i+1} - \rho^i}{\Delta t_{i+1}} + \boldsymbol{\sigma}'^{n+1/2} : \dot{\mathbf{e}}^{n+1/2}, \tag{40}$$

$$\boldsymbol{\sigma}^{i+1} = \boldsymbol{\sigma}'^{i+1} - (\sigma_h^{i+1} + p_{bv}^{i+1})\boldsymbol{I}. \tag{41}$$

For simplicity, the artificial viscosity in Eqs. (40) and (41) at step i is approximated as the viscosity calculated at step $i - 1/2$. The introduction of the artificial viscosity doesn't influence the calculated results in this article considerably. In particular, only the HEL spike changes slightly when we adjusted the values of the scale factors of the artificial viscosity.

3. Results and discussion

The proposed model is implemented as a VUMAT into the Abaqus/Explicit finite element code. Using the model, we modeled the preheated plate-impact experiments performed by Zaretsky (2009) and Zaretsky and Kanel (2014, 2015, 2016, 2017) in recent years. In these experiments, BCC metals are preheated to a specified temperature and then impacted by a flyer with a velocity of up to several hundred meters per second accelerated by a gas gun. To avoid lateral rarefaction, the diameter of the samples perpendicular to the loading direction is much larger than the thickness along the loading direction. Under this condition, the planar impact experiment is usually treated as a plane strain problem. Particle velocities at the free surface are recorded by using Velocity Interferometer System for Any Reflector (VISAR).

A three-dimensional finite element computational model is developed with a mesh size of 0.5 μm. The grain size is set as 30 μm. The orientation distribution of the grain lattice of relatively thick samples, 1.0 and 2.0 mm, is randomly chosen, while that of relatively thin samples, 0.25 and 0.5 mm, is adjusted to fit the experimental results. There is only one mesh layer in the direction perpendicular to the loading direction, and the displacement in the perpendicular direction is set as zero to simulate the uniaxial strain state. The flyer plate is endowed with initial velocity and impacts the sample at initial time. Under this condition, global strain rate is enforced by the impact velocity.

Model parameters are determined by fitting the evolution of the critical features of the velocity profiles, including the HEL and the plastic shock front. The dislocation-based constitutive model has 14 adjustable parameters. Among which, 4 are critical to HEL evolution: α_{mult}, B_{pin}, α_{HN}, and χ; the others are set as equal values for different materials.

α_{mult} and B_{pin} are determined by fitting experimental results at room temperature. With the same α_{mult} and B_{pin}, calculated results match well with experimental results at different applied stresses and those obtained from samples with different thicknesses at room temperature, as shown in Figs. 2 and 3. α_{HN}, and χ are determined by fitting experimental results at elevated temperature. Here, the texture to simulate experiments of thicker samples is randomly chosen, while that of thinner vanadium and tantalum samples are set as ⟨111⟩ preferential and ⟨100⟩ preferential, respectively, which is acceptable because fewer grains in a thinner sample cannot maintain a random distribution of grain orientation.

We can see from Figs. 2 and 3 that model-generated results match well with experimental results at different applied stresses, at different temperatures, and with those obtained from samples with different thicknesses, which verifies the validity of this model for addressing the temperature dependence of the mechanical response at shock loading.

Subsequently, we simulated the velocity profiles of W, Fe, and Mo using this model, as shown in Fig. 4. The temperature dependence of the dynamic yield stress of five BCC metals using this model is displayed in Fig. 5. Figs. 4 and 5 indicate that the calculated results with this model are in good agreement with experimental results, including the temperature dependence of the dynamic yield stress and the elastic–plastic wave characteristics, over wide temperature range, which suggests that this model is effective for shock-loaded BCC metals even at elevated temperature.

Given that dynamic yielding is dominated by plastic deformation, we can now explore the underlying mechanisms of the dynamic yield stress from the controlling mechanisms of dislocation evolution and twinning evolution. How dislocation evolution and twinning evolution influence the dynamic yield stress, respectively, is discussed in the

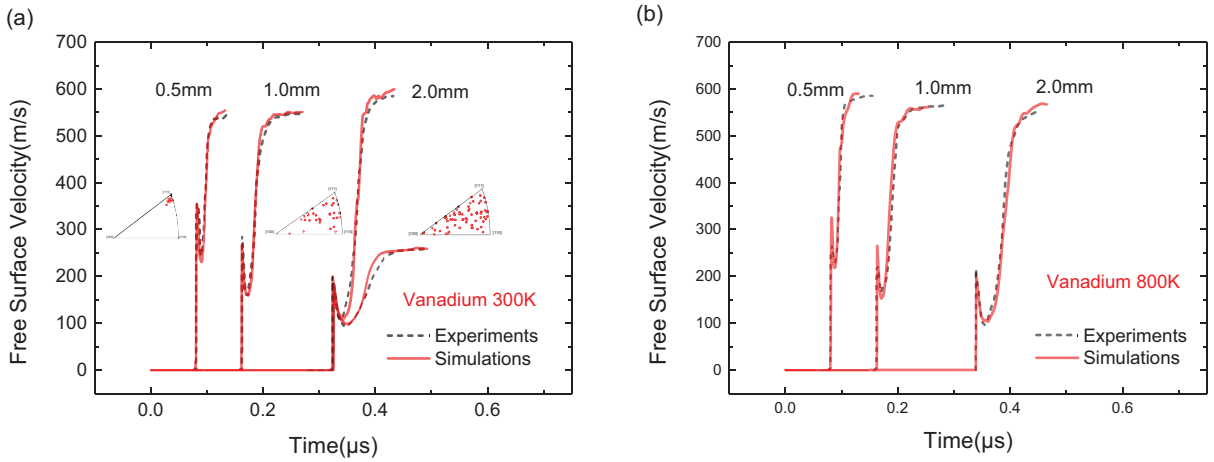

Fig. 2. Comparison between experiments and simulations for vanadium: (a) 300 K; (b) 800 K. Red solid lines refer to calculated time histories of the free surface velocity and black dashed lines refer to experimental results (Zaretsky and Kanel, 2014). During the simulations, both the evolution of twinning and that of dislocations are taken into account. The ⟨111⟩ preferential texture is chosen to fit the experiments with the 0.5-mm sample, while a random distributed texture is chosen to simulate experiments with thicker samples; the insets present the chosen texture. The same texture is chosen to simulate samples of the same thickness at different temperatures. (For interpretation of the references to color in this figure legend, the reader is referred to the web version of this article.)

following.

3.1. Effect of twinning on the dynamic yield stress of vanadium

In this study, we aimed to address the mechanical response of a series of experiments performed by Zaretsky and Kanel in recent years. In these experiments, twinning is only observed in the recovered vanadium sample, but not in other BCC metals. Therefore, we mainly discuss the effect of twinning on the dynamic yield stress of vanadium.

There are three parameters used to describe the stress dependence of the twinning shear rate in the phenomenological model used in this article: the twinning threshold stress τ_{tw}, the reference twinning shear rate $\dot{\gamma}_{tw}^{0}$, and the rate-sensitivity power coefficient r. The twinning threshold stress of vanadium is obtained from Ojha and Sihitogl (2014), while the reference twinning shear rate and the rate-sensitivity power coefficient are adjusted to fit the experimental results based on the values of tantalum (Florando et al., 2013). Parameters for the twinning model used in this article are listed in Table 8.

Two kinds of calculations are performed: one using the twinning model, and another with no twinning, to study the effect of twinning. To strengthen the effect of twinning on the mechanical response, the reference twinning shear rate of tantalum is adjusted to 100 s^{-1}. A comparison between calculated results of vanadium with twinning considered and those without twinning considered is displayed in Fig. 6. It is suggested by Fig. 6 that the effect of twinning is significant at the location near the impact surface and is almost negligible at a location ~1.0 mm away from the impact surface. Calculated results also indicate that the twinning shear rate drops significantly, by about two orders of magnitude, when the shock wave propagates from 0.25 to 1.75 mm, as shown in Fig. 7(a). The calculated spatial distribution of twinning is in accordance with that in recovered samples (Meyers et al., 2009; Pang et al., 2018). We can learn from Pang et al. (2018), as shown in Fig. 7(b), that the twinning area fraction along ⟨001⟩ and ⟨111⟩ is significant near the impact surface but is almost negligible at a location of >0.5 mm away from the impact surface and that the twinning area fraction along ⟨011⟩ drops to <10% at a location of >1.5 mm away from the impact surface.

As displayed in Fig. 8(a), the calculated results for vanadium at elevated temperature exhibit the same spatial distribution as that at room temperature, suggesting that twinning shear deformation does not

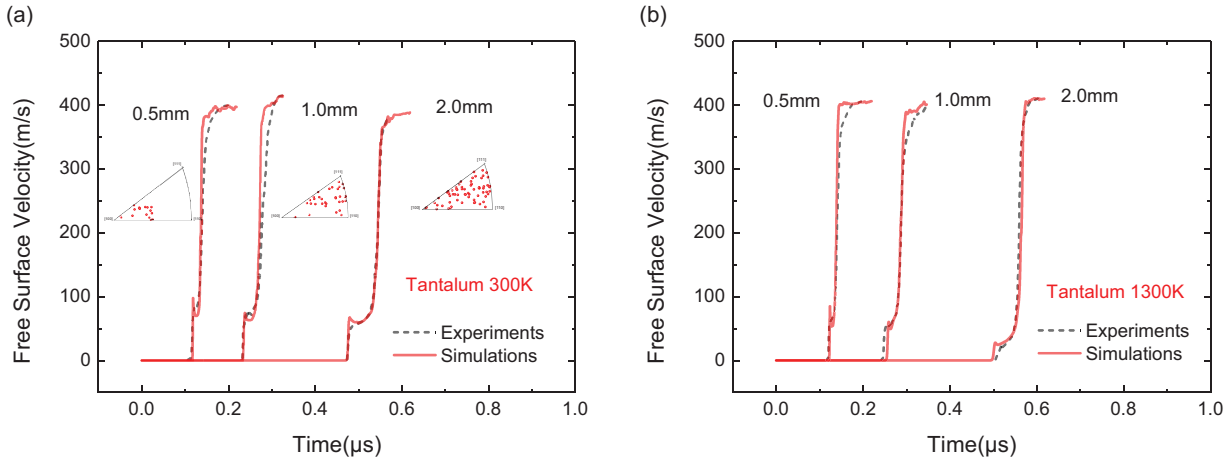

Fig. 3. Comparison between experiments and simulations for tantalum: (a) 300 K; (b) 1300 K. Red solid lines refer to calculated time histories of the free surface velocity and black dashed lines refer to experimental results (Zaretsky and Kanel, 2014). During the simulations, only the evolution of dislocations is taken into account. The ⟨100⟩ preferential texture is chosen to fit the experiments with the 0.5-mm sample, whereas a random distributed texture is chosen to simulate experiments of thicker samples; the insets present the chosen texture. (For interpretation of the references to color in this figure legend, the reader is referred to the web version of this article.)

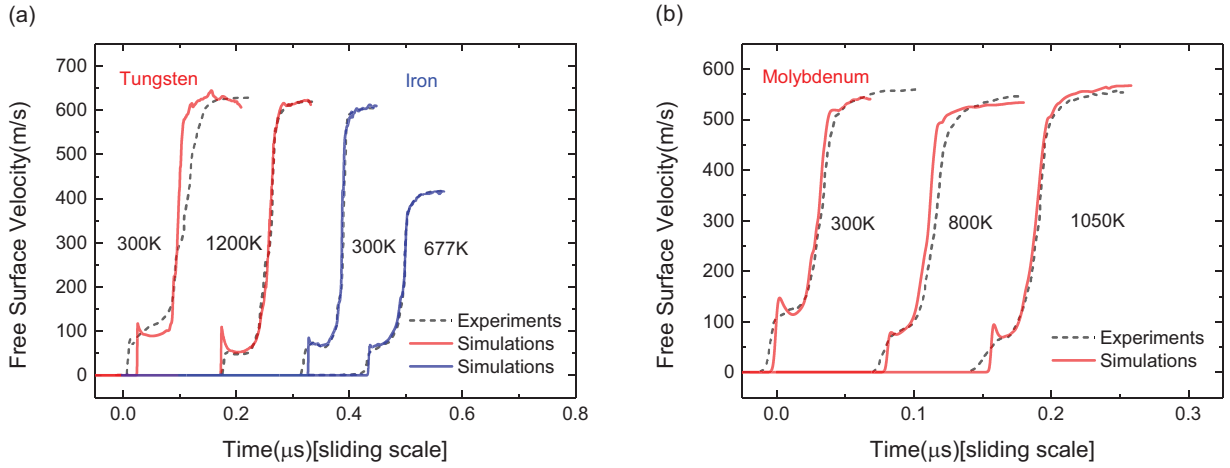

Fig. 4. Comparison between calculated time histories of the free surface velocity of W, Fe, and Mo at different temperatures and experimental results (Zaretsky, 2009; Zaretsky and Kanel, 2015, 2016, 2017): (a) 2 mm Tungsten and 2 mm Iron; (b) 1 mm Molybdenum.

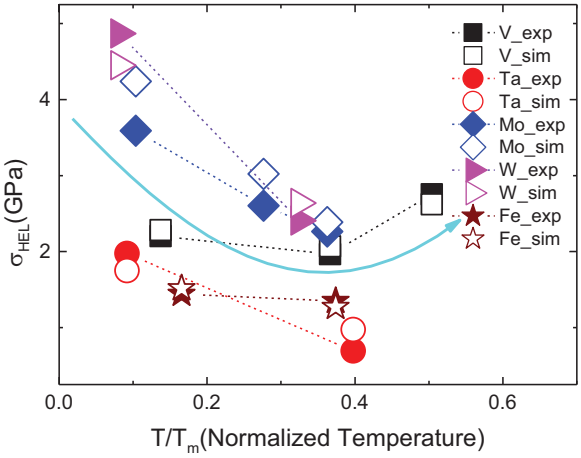

Fig. 5. Comparison of calculated temperature dependence of the dynamic yield stress and experimental results. The dynamic yield stress, $\sigma_{HEL} = \rho_0 C_l u_{HEL}$, where ρ_0 is the initial material density, C_l is the longitudinal sound speed, and u_{HEL} is the particle velocity at the HEL minimum, is the stress at the HEL minimum. Solid symbols refer to experimental results while open symbols refer to calculated results. The different shapes of symbols refer to results for different materials.

Table 8
Twinning model parameters.

Material	V	Ta
τ_{tw} (MPa)	220	300
$\dot{\gamma}_{tw}^{0}$ (s^{-1})	1	100
r	0.1	0.1

significantly influence the temperature dependence of the dynamic yield stress. The temperature dependence of twinning shear deformation can be understood from the temperature insensitivity of Peierls stress for partial dislocations, which determines the twinning threshold stress. Given that Peierls stress for perfect dislocations drops quickly with increasing temperature (Hirth and Lothe, 1968), temperature insensitivity of the twinning threshold stress leads to more significant dislocation shear deformation and less significant twinning deformation at higher temperature. As shown in Fig. 8(b), the twinning deformation rate decreases with increasing temperature, whereas the dislocation shear deformation rate increases with increasing temperature. Nonetheless, the effect of twinning deformation on the temperature dependence of the dynamic yield stress is still difficult to distinguish from the effect of dislocations because the reduction of plastic deformation accommodated by twinning can be accommodated by dislocations at higher temperature.

3.2. Effect of dislocation evolution on the temperature dependence of the dynamic yield stress

As analyzed above, the influence of twining on the dynamic yield stress is only significant near the impact surface. Because the common temperature dependence of the dynamic stress does not depend on spatial size, we can thus attribute the temperature dependence of the dynamic yield stress to dislocation evolution, including dislocation motion and dislocation generation. In the following, we aim to address the temperature dependence of the dynamic yield stress from the viewpoint of dislocation motion and dislocation generation.

3.2.1. Dislocation motion mechanisms

In the classical picture, Peierls stress marks the transition from thermally activated glide of dislocations below Peierls stress to the phonon drag mechanism above Peierls stress, and thermal softening behaviors are usually attributed to thermally activated dislocation motion. For a weak shock-loading problem, the applied stress induced by shock compression exceeds the Peierls stress quickly, leading to an elimination of thermally activated glide of dislocations and to phonon drag dominating dislocation motion. Thus the dislocation velocity is mainly controlled by Peierls stress and phonon drag. As temperature increases, the drop of Peierls stress makes it easier for dislocations to move, while the growth of phonon drag makes it more difficult. The interference is that Peierls stress with phonon drag may indeed result in different temperature dependences of the dynamic yield stress.

First, let us neglect temperature-dependent dislocation generation, i.e., TA-HN, to ascertain whether the abovementioned two classical mechanisms i.e., Peierls stress and phonon drag, that control dislocation motion are responsible for the temperature-dependent behaviors of the dynamic strength of shock-loaded BCC metals. As shown in Fig. 10(a), the calculated velocity profiles of tantalum and vanadium at room temperature are in good agreements with temperature, and the thermal softening behavior of tantalum is well reproduced. However, the calculated HEL minima of vanadium at 1100 K and at 800 K are much smaller than experimental values, and the HELs show a temperature insensitive tendency at <1100 K. From the viewpoint of dislocation motion, dislocation velocities, as displayed in Fig. 9, at different temperatures exhibit temperature insensitivity when subjected to shear stress at several hundreds of MPa because the phonon drag

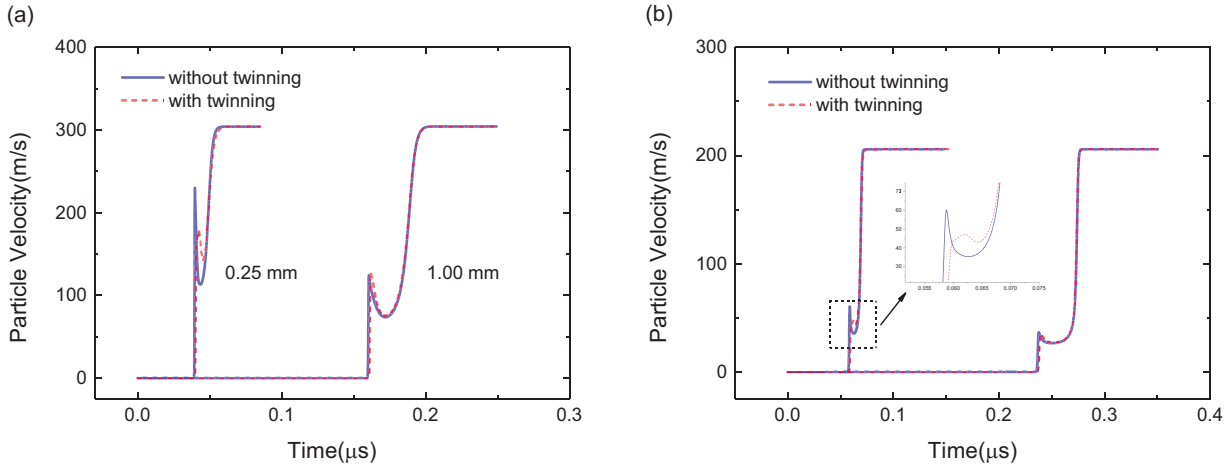

Fig. 6. Comparison between calculated results with twinning and those without twinning: (a) calculated results of vanadium at 300 K; (b) calculated results of tantalum at 300 K. Blue solids lines refer to calculated results without twinning considered, while red dashed lines refer to calculated results with twinning considered. (For interpretation of the references to color in this figure legend, the reader is referred to the web version of this article.)

hardening is counterbalanced by the rapid drop of Peierls stress. Apparently, a constitutive model in which only the temperature dependence of dislocation motion is taken into account is incapable of accurately capturing the constitutive behavior of shock-loaded BCC vanadium at elevated temperature.

3.2.2. *Thermally activated dislocation generation*

In addition to dislocation motion, dislocation generation has also been proposed as the primary contributing factor to the dynamic strength at high strain rate. To the best of our knowledge, the temperature-dependent behavior of dislocation generation has not been addressed in the literature. In this study, temperature-dependent dislocation generation is mainly attributed to TA-HN. HN occurs when the applied stress approaches the nucleation strength, $\sim G/15$ for most metals (Hirth and Lothe, 1968), and is difficult to achieve. According to calculations, the shear stress induced by a shock velocity of several hundred meters per second is much less than the nucleation strength. Under this condition, HN is thermally activated. Owing to its thermal activation property, TA-HN is of high temperature sensitivity and high stress sensitivity. As temperature increases, decrease in activation energy and increase in thermal fluctuations make it easier for HN to occur.

Subsequently, we performed calculations using a model with TA-HN considered. The calculated substructure evolution rate of vanadium is displayed in Figs. 11(a) and (b). As shown in Figs. 11(a) and (b), temperature = dependent dislocation generation is strongly strengthened by TA-HN. In particular, the HN rate at 300 K is almost negligible compared to the multiplication rate, while the HN rate grows quickly with temperature and is about two orders of magnitude larger than the multiplication rate at 1100 K. A higher HN rate results in a higher dislocation density at higher temperature. As shown in Fig. 12, the total dislocation densities behind the shock front are $\sim 10^{15}$ and $\sim 10^{16}$ m^{-2} at 300 K and 1100 K, respectively.

A comparison between the calculated velocity profiles with TA-HN considered and experimental results is displayed in Fig. 10(b). As shown in Fig. 10(b), the calculated results at elevated temperature with HN considered show a higher HEL minimum and match better with experimental results than those without HN considered, which indicates that TA-HN is responsible for the thermal hardening behavior of the dynamic yield stress of BCC vanadium at elevated temperatures. Besides that, we can also learn that TA-HN results in a slight decrease of the HEL spike at elevated temperature, but it is not significant, which indicates that the primary contributing factor to the temperature dependence of HEL spikes are dislocation motion and not dislocation generation. Nonetheless, from the viewpoint of dislocation generation, TA-HN, providing more dislocations for plastic slip, is still a thermal softening mechanism but not a thermal hardening mechanism.

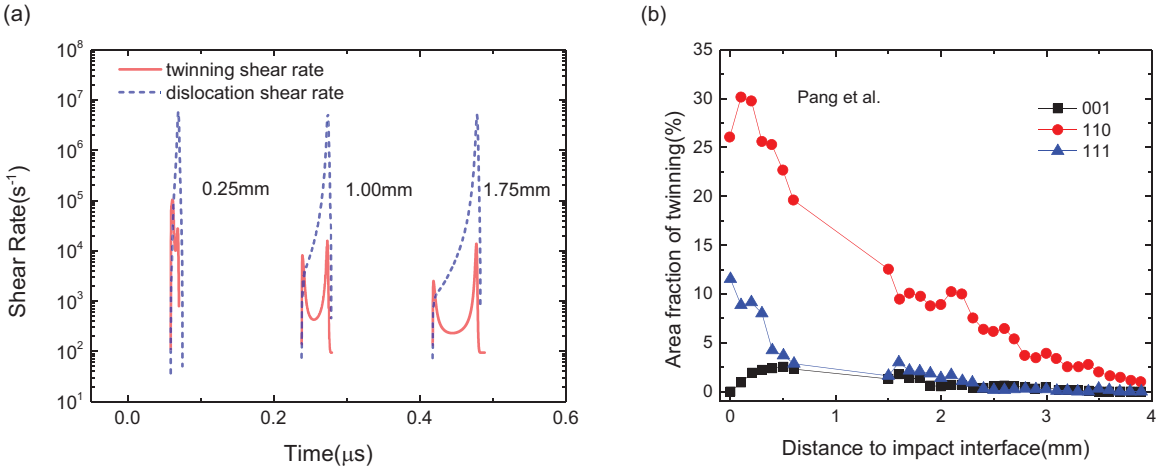

Fig. 7. Time history of the shear rate: (a) Calculated time histories of the shear rate of tantalum at different locations along the loading direction. (b) Experimentally observed spatial distribution of twinning area fraction of shock-loaded tantalum along the loading direction (Pang et al., 2018). (For interpretation of the references to color in this figure legend, the reader is referred to the web version of this article.)

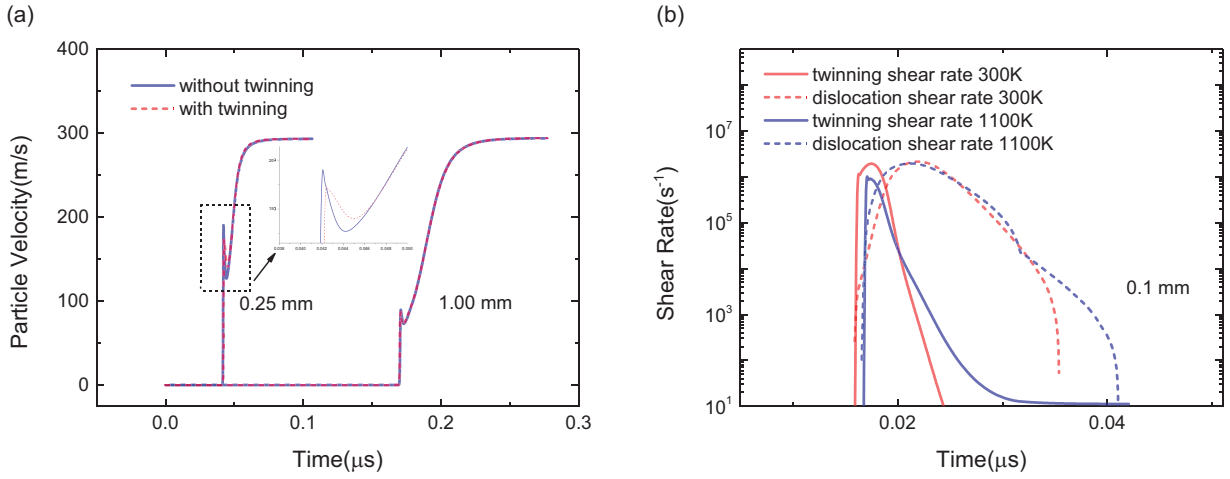

Fig. 8. Calculated results at 1100 K: (a) spatial distribution of the velocity profiles; (b) comparison of calculated shear rates at 300 K and that at 1100 K. (For interpretation of the references to color in this figure legend, the reader is referred to the web version of this article.)

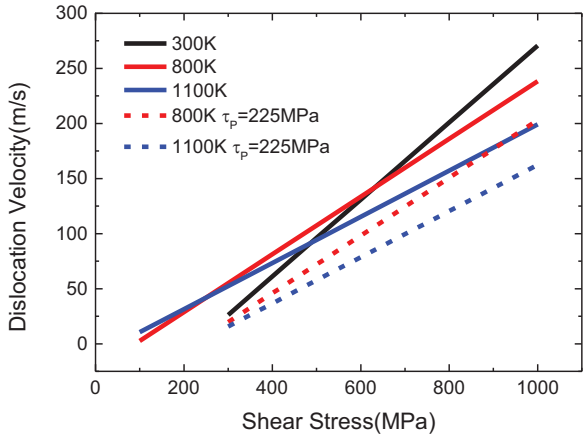

Fig. 9. Dislocation velocity vs. shear stress. Solid lines refer to dislocation velocities calculated by using the real Peierls stress and the phonon drag coefficient, while dashed lines refer to those calculated by using the room temperature Peierls stress and the real phonon drag coefficient.

3.2.3. Forest hardening

Newly generated dislocations not only serve as plasticity carriers but also as obstacles for other dislocations to move via dislocation–dislocation interactions, namely, the forest hardening mechanism (Madec and Kubin, 2017). Forest hardening and Peierls stress serve as the mechanical threshold stress, also known as the CRSS, for a dislocation to move together. Forest hardening has been proposed as providing the primary resistance to dislocations moving in FCC metals owing to the relatively low Peierls stress of FCC metals, while the influence of forest hardening on dislocation motion has been proposed as insignificant in BCC metals because the effect of forest hardening on dislocation motion is almost negligible compared to the relatively high Peierls stress of BCC metals. Moreover, existing studies at moderate strain rates indicate that the plastic hardening of most BCC metals is barely influenced by temperature and contributes to the athermal part of the flow stress (Voyiadjis and Abed, 2005). However, massively generated dislocations by TA-HN at high strain rate make the effect of forest hardening on dislocation motion significant in BCC metals, especially at relatively high temperature.

We can learn from Fig. 12 that immobile dislocation density at 1100 K is about three orders of magnitude higher than that at 300 K because of the temperature sensitivity of TA-HN. Here, the influence of the mobile coefficient χ, which defines the mobile portion of nucleated dislocations after gliding a constant distance, should be emphasized. In

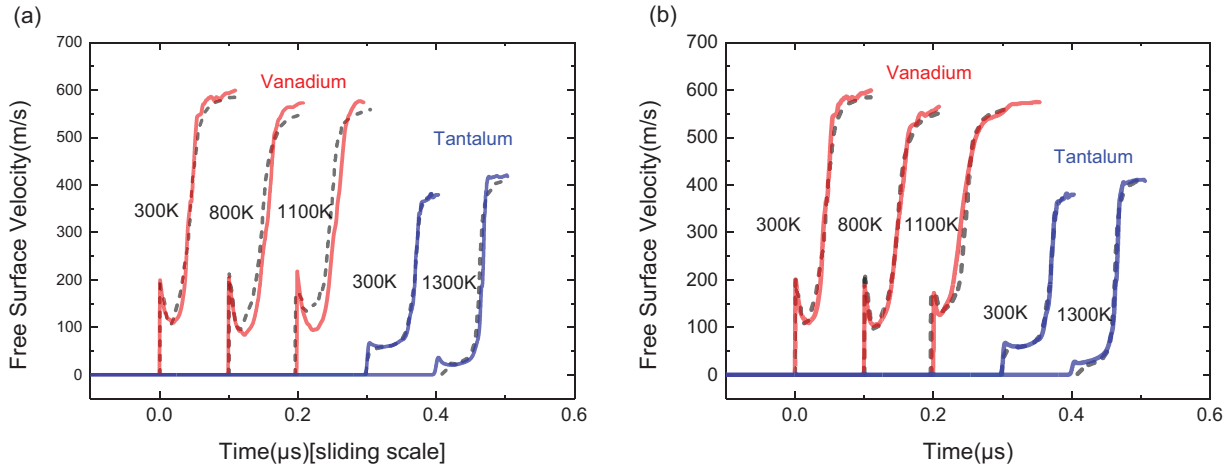

Fig. 10. Comparison between calculated time histories of the free surface velocity for tantalum and vanadium at different temperatures and experimental results (Zaretsky and Kanel, 2014): (a) without HN; (b) with HN. Dashed lines refer to experimental results, and solid lines refer to calculated results. There are 67 grains along the loading direction, and the orientation of the grains is randomly chosen.

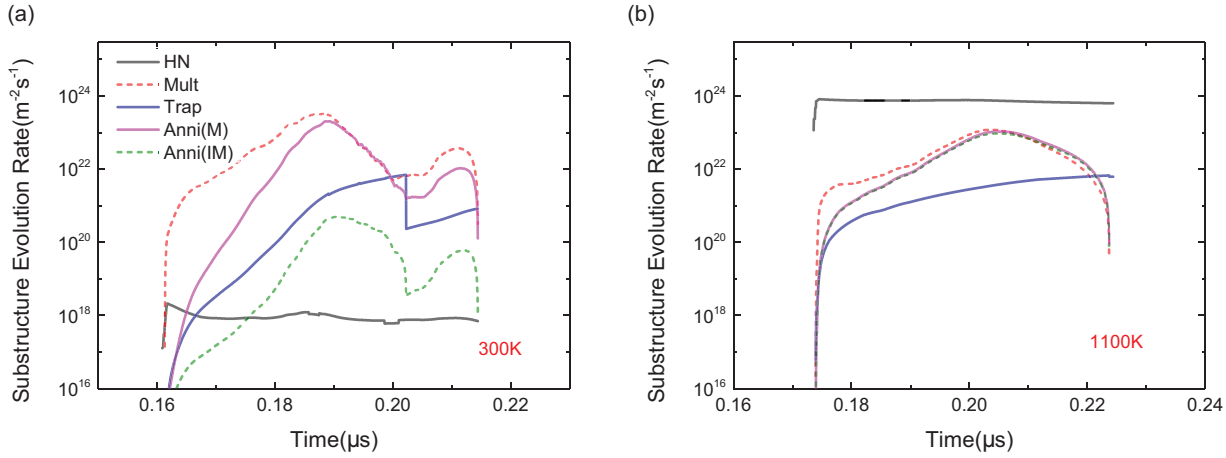

Fig. 11. Calculated dislocation substructure evolution rate at a location 1.0 mm away from the impact surface of vanadium at different temperatures: (a) 300 K; (b) 1100 K. The black solid line refers to the time history of the HN rate, the red solid line refers to the time history of the dislocation multiplication rate, the blue solid line refers to the time history of the dislocation trapping rate, and dashed lines refer to time histories of the dislocation annihilation rate. (For interpretation of the references to color in this figure legend, the reader is referred to the web version of this article.)

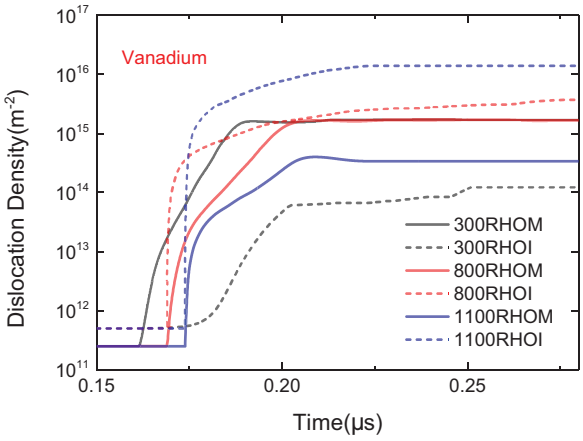

Fig. 12. Calculated time histories of dislocation density in vanadium at a location about 1.0 mm away from the impact surface. Lines of different colors refer to dislocation density at different temperatures. Solid lines refer to mobile dislocation density, while dashed lines refer to immobile dislocation density.

the simulations, the value of χ, determined by fitting the HEL at elevated temperatures is adjusted to be relatively small, which results in most of nucleated dislocations becoming immobile after gliding a constant distance and contributing to the forest hardening. If we adjust the coefficient to a larger value, greater numbers of dislocations generated by TA-HN participate in plastic slip, which helps to decrease the HEL, and thermal hardening behavior of the HEL minima would never emerge. The small value of the mobile coefficient can be understood from the mobility of edge dislocations. The mobility of edge dislocations in a BCC metal is much higher than that of screw dislocations, which results in most of the edge dislocations becoming immobilized quickly when encountering grain boundaries or other obstacles (Cui et al., 2016) and serve as obstacles for other dislocations.

The forest hardening mechanism, described by the Taylor relation, can be reflected by the evolution of the CRSS. As shown in Fig. 13(a) and (b), the CRSS at room temperature almost does not evolve, whereas the CRSS at elevated temperature increases considerably. The CRSS of vanadium at 1100 K even exceeds that at 300 K before the plastic wave arrives. Given that Peierls stress is determined by the ambient temperature, thermal hardening of the CRSS is thus attributed to forest hardening. More dislocations generated at higher temperatures owing to the thermal activation property of HN lead to thermal hardening of the dislocation–dislocation interaction resistance and thermal hardening of the dynamic yield stress.

3.2.4. Forest hardening and Peierls stress

As analyzed above, different temperature dependences of the dynamic yield stress result from different temperature dependences of the CRSS, including the contribution of Peierls stress and forest hardening. Though forest hardening plays the same role as Peierls stress does in dislocation motion, their temperature effects on dislocation motion happen to be opposite to each other. As temperature increases, a rapid decrease of Peierls stress contributes to thermal softening of the CRSS, whereas growth of the foresting hardening induced by HN contributes to thermal hardening of the CRSS.

At relatively low temperature, Peierls stress of a BCC metal drops sharply with increasing temperature, and the growth of forest hardening induced by TA-HN is not enough to make up for the loss of the Peierls stress because of the relatively low HN rate. Thus Peierls stress controls the temperature dependence of the CRSS, leading to a thermal softening behavior of the dynamic strength. That is why almost all BCC metals exhibit thermal softening behaviors at relatively low temperature. As temperature increases, Peierls stress becomes relatively low, as does the temperature derivative of Peierls stress. Meanwhile, forest hardening induced by TA-HN grows quickly with temperature. In particular, the temperature derivative of the Peierls stress of vanadium is almost negligible compared to that of forest hardening at >800 K. Moreover, phonon drag also contributes to the thermal hardening behavior of the dynamic yield stress. Consequently, vanadium exhibits thermal hardening behavior at >800 K. For other BCC metals, Peierls stress and its temperature derivative are still significant over the same temperature range and control the temperature-dependent behavior of the CRSS. Consequently, these metals still exhibit thermal softening even at temperatures of >1000 K.

3.2.5. Prediction of the temperature dependence of the dynamic yield stress at higher temperature

Thermal hardening has only been observed in vanadium but has not yet been observed in other BCC metals. Based on the above analysis, it is expected that thermal hardening behavior can also be observed in other shock-loaded BCC metals at higher temperatures at which Peierls stress and its temperature derivative for a BCC metal almost vanish. To verify this expectation, we simulated the shock-loading response of four typical BCC metals, vanadium, tantalum, molybdenum, and tungsten, over a wider temperature range, as shown in Fig. 14. It is numerically found that all metals exhibit thermal softening behaviors at relatively low temperature, whereas thermal hardening behaviors of the dynamic

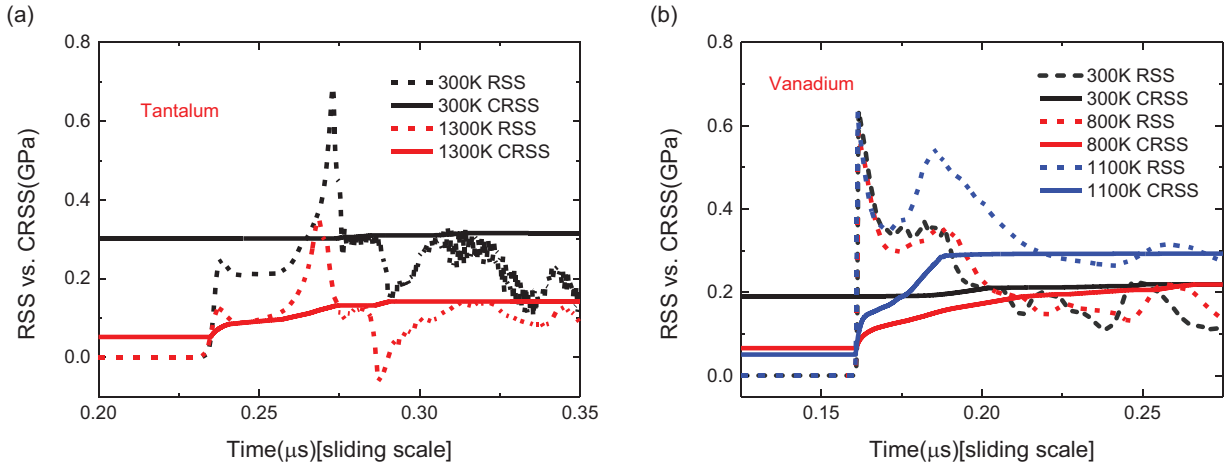

Fig. 13. Calculated time histories of RSS and CRSS at different temperatures: (a) tantalum; (b) vanadium. Solid lines refer to time histories of CRSS, while dashed lines refer to time histories of RSS. Lines of different colors refer to different temperatures.

yield stress occur in all four metals except Ta at relatively high temperature, as shown in Fig. 14(b).

As analyzed in Section 3.2.4, the thermal softening behavior of the dynamic yield stress at relatively low temperature is due to the rapid drop of Peierls stress, while thermal hardening behavior of the dynamic strength at relatively high temperature is mainly due to forest hardening induced by TA-HN, leading to thermal hardening of the CRSS. However, it is demonstrated by Fig. 14 that the CRSS of vanadium and molybdenum first increase and finally decrease with temperature at relatively high temperature, which indicates that the thermal hardening behaviors of vanadium and molybdenum at higher temperature, above ~$0.5T_m$, are no longer due to forest hardening but rather to phonon drag. The Taylor relation indicates that the decrease of the CRSS above $0.5T_m$ is due to the decrease of the shear modulus and the saturation of dislocation density.

The role of saturation dislocation density should be emphasized when addressing the mechanical response at elevated temperature. We used the saturation dislocation density model proposed by Barton et al. (2011) to determine the upper limit of dislocation density at a specified strain rate. At relatively high temperature, dislocation density grows sharply and becomes saturated quickly even before the HEL minima, as shown in Fig. 15. Thus the role of forest hardening on the behavior of the HEL minimum at relatively high temperature is no longer significant. The evolution of the CRSS is completely determined by the saturation dislocation density, which is determined by the instantaneous strain rate. We can see from Fig. 15 that dislocation density becomes saturated quickly at elevated temperature, and the dislocation

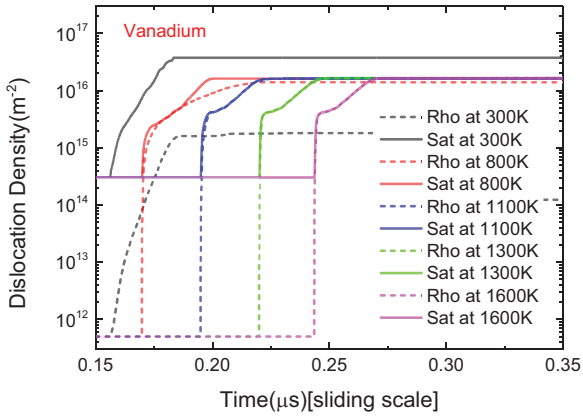

Fig. 15. Calculated dislocation densities of vanadium at different temperatures at a location 1.0 mm away from the impact surface. Dashed lines denote total dislocation density, while solid lines denote saturation dislocation density. Different colors refer to different temperatures.

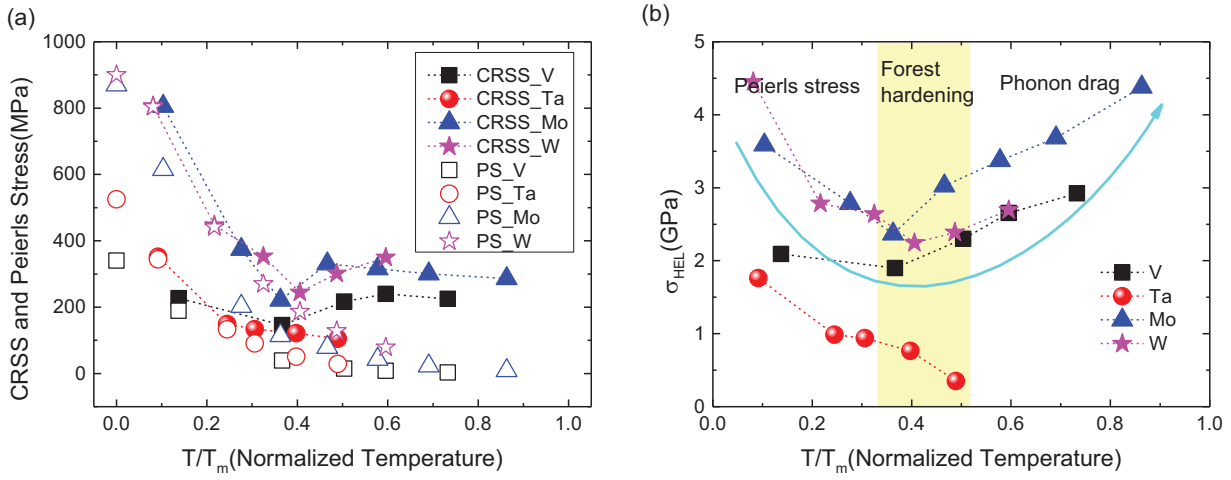

Fig. 14. Calculated CRSS in the sample and dynamic yield stress at the free surface at different temperatures. (a) Comparison of Peierls stress and CRSS at a location 1.0 mm away from the impact surface. Solid symbols refer to the calculated CRSS, while open symbols refer to Peierls stress. (b) Dynamic yield stress at the free surface. Different symbols refer to mechanical quantities of different materials.

density evolves just as the saturation dislocation density does.

Thermal hardening behavior is not found in Ta because the shock velocity in Ta is relatively lower than those in other metals, leading to a relatively lower HN rate. Moreover, phonon drag hardening of Ta is regarded as temperature insensitive, so also does not contribute to thermal hardening behavior of the dynamic yield stress.

Above all, the temperature dependence of the dynamic yield stress can be classified into three regions according to temperature. At relatively low temperature, the rapid drop of Peierls stress dominates the temperature dependence of the CRSS, leading to a thermal softening behavior of the dynamic strength. At relatively high temperature, forest hardening induced by HN dominates the CRSS and contributes to thermal hardening behavior of the dynamic strength. At even higher temperature, the temperature dependence of forest hardening almost vanishes because dislocation density becomes saturated quickly because of the high HN rate, and the temperature dependence of the dynamic strength is a result of interference between phonon drag and Peierls stress.

4. Summary and conclusions

We have numerically investigated the temperature-dependent behaviors of the dynamic yield stress of shock-loaded BCC metals through a dislocation-based constitutive model. The aim of this work is to gain insight into the underlying mechanisms that control the temperature dependence of the dynamic yield stress. To describe the shock-loading response of BCC metals at high strain rate and high temperature correctly, a dislocation-based constitutive model in which controlling mechanisms of dislocation motion, dislocation generation, and twinning are comprehensively considered is established. Through numerical simulations with this model, we have quantitatively reproduced the experimental results, including the thermal hardening behavior of vanadium at elevated temperature and the thermal softening behaviors of other BCC metals.

It is found that the influence of twinning on the dynamic yield stress of shock-loaded BCC metals and its temperature dependence is almost negligible and four dislocation-associated mechanisms, including Peierls stress, phonon drag, forest hardening, and TA-HN, are demonstrated to significantly influence the temperature dependence of the dynamic yield stress of shock-loaded BCC metals. In the classical picture, Peierls stress and the phonon drag mechanism, which control dislocation motion, are the fundamental origin of the temperature dependence of the dynamic yield stress. In this article, Peierls stress has been proven to be the primary contributing factor to the thermal softening behavior of BCC metals, in accordance with the conclusion of D3P simulations (Gurrutxaga-Lerma et al., 2017), while the temperature effect of phonon drag on the dynamic yield stress is counterbalanced by the rapid drop of Peierls stress and is almost negligible at relatively low temperature. The novelty of this work lies in the forest hardening induced by TA-HN having been proposed as the primary contributing factor to the experimentally observed thermal hardening behavior of vanadium. The forest hardening mechanism is usually regarded as insignificant and insensitive to temperature in BCC metals. However, it is suggested by this work that forest hardening becomes significant at the elevated temperatures at which Peierls stress almost vanishes and that the temperature effect of TA-HN results in the forest hardening mechanism being temperature sensitive and increasing with increasing temperature. What excites us is that the numerical analysis predicts that this thermal hardening mechanism is also suitable for other BCC metals, e.g., tungsten and molybdenum, at temperatures between $0.35T_m$ and $0.50T_m$, and that phonon drag hardening contributes more significantly to the dynamic strength at even higher temperature, above $\sim 0.50T_m$.

Declaration of Competing Interest

We declare that we have no financial and personal relationships with other people or organizations that can inappropriately influence our work, there is no professional or other personal interest of any nature or kind in any product, service and/or company that could be construed as influencing the position presented in, or the review of, the manuscript entitled “Numerical investigation of the temperature dependence of dynamic yield stress of typical BCC metals under shock loading with a dislocation based constitutive model”.

Acknowledgment

S. L. Yao has benefited from fruitful discussions with Prof. R. W. Armstrong, Prof. J. Wang (University of Nebraska-Lincoln), and Dr. Y. N. Cui (Tsinghua University). The authors would like to thank Prof. W. Q. Wang, Prof. P. Li, Prof. H. Y. Geng, and Dr. L. Y. Kong for useful remarks and Dr. S. Chen for providing language help. This work was supported by the Science Challenge Project (Grant No. TZ2018001), the Foundation of the President of the China Academy of Engineering Physics (Grant No. 201402084), and the National Natural Science Foundation of China (Grant No. 11532012).

References

Abaqus Analysis User’s Guide, 2016.
Adams, J.J., et al., 2006. Elastic constants of monocrystal iron from 3 to 500 K. J. Appl. Phys. 100, 113539.
Armstrong, R.W., Arnold, W., Zerilli, F.J., 2009. Dislocation mechanics of copper and iron in high rate deformation tests. J. Appl. Phys. 105, 023511.
Austin, R.A., McDowell, D.L., 2012. Parameterization of a rate-dependent model of shock induced plasticity for copper, nickel, and aluminum. Int. J. Plast. 32-33, 134–154.
Barton, N.R., et al., 2011. A multiscale strength model for extreme loading conditions. J. Appl. Phys. 109, 073501.
Benson, D.J., 1992. Computational methods in Lagrangian and Eulerian hydrocodes. Comput. Methods Appl. Mech. Eng. 99, 235–394.
Bringa, E.M., et al., 2005. The atomistic modeling of wave propagation in nanocrystals. JOM J. Miner. Metals Mater. Soc. 57, 67–70.
Chen, Z.M., Mrovec, M., Gumbsch, P., 2013. Atomistic aspects of 1/2(111) screw dislocation behavior in alpha-iron and the derivation of microscopic yield criterion. Model. Simul. Mater. Sci. Eng. 21, 055023.
Crichton, W.A., et al., 2016. High-temperature equation of state of vanadium. High Press. Res. 36, 16–22.
Cui, Y., Po, G., Ghoniem, N., 2016. Temperature insensitivity of the flow stress in body-centered cubic micropillar crystals. Acta Mater. 108, 128–137.
De, S., Zamiri, A.R., Rahul, 2014. A fully anisotropic single crystal model for high strain rate loading conditions with an application to alpha-RDX. J. Mech. Phys. Solids 64, 287–301.
Dickinson, J.M., Armstrong, P.E., 1967. Temperature dependence of the elastic constants of molybdenum. J. Appl. Phys. 38, 602–606.
Florando, J.N., et al., 2013. Analysis of deformation twinning in tantalum single crystals under shock loading conditions. J. Appl. Phys. 113, 083522.
Greiner D., J., et al., 1979. Single-crystal elastic constants of vanadium and vanadium with oxygen additions. J. Appl. Phys. 50, 4394–4398.
Gurrutxaga-Lerma, B., et al., 2017. The effect of temperature on the elastic precursor decay in shock loaded FCC aluminum and bcc iron. Int. J. Plast. 96, 135–155.
Hansen L., B., et al., 2013. A dislocation-based multi-rate single crystal plasticity model. Int. J. Plast. 44, 129–146.
Hirth, J.P., Lothe, J., 1968. Theory of Dislocations. Mcgraw-Hill, New York, pp. 757–759 p.811.
Hirth, J.P., Zbib, H.M., Lothe, J., 1998. Forces on high velocity dislocations. Model. Simul. Sci. Eng. 6, 165–169.
Jamal, M., et al., 2014. Computational constants of cubic crystals. Comp. Mater. Sci. 95, 592–599.
Johnston, W.G., Gilman, J.J., 1960. Dislocation multiplication in lithium-fluoride of crystals. J. Appl. Phys. 31, 632–643.
Kanel, G.I., 2014. Unusual behavior of usual materials in shock waves. J. Phys. Conf. Series 500, 1–10.
Katahara, K.W., Manghnani, M.H., 1976. Pressure derivatives of the elastic moduli of niobium and tantalum. J. Appl. Phys. 47, 434–439.
Krasnikov, V.S., Mayer, A.E., Yalovets, A.P., 2011. Dislocation based high-rate plasticity model and its application to plate-impact and ultrashort irradiation simulations. Int. J. Plast. 27, 1294–1308.
Kuksin, A.Yu, Yanilkin, A.V., 2013. Atomistic simulation of the motion of dislocations in metals under phonon drag conditions. Phys. Solid State 55, 1010–1019.
Kushwah, S.S., Sharma, M.P., Tomar, Y.S., 2003. An equation of state for molybdenum and tungsten. Phys. B 339, 193–197.
Lennon, A.M., Ramesh, K.T., 2004. The influence of crystal structure on the dynamic behavior of materials at high temperatures. Int. J. Plast. 20, 269–290.
Lloyd, J.T., et al., 2014. Simulation of shock wave propagation in single crystal and polycrystalline aluminum. Int. J. Plast. 60, 118–144.
Luscher, D.J., et al., 2013. A model for finite-deformation nonlinear thermomechanical

response of single crystal copper under shock conditions. J. Mech. Phys. Solids 61, 1877–1894.
Madec, R., Kubin, L.P., 2017. Dislocation strengthening in FCC metals and in BCC metals at high temperatures. Acta Mater. 126, 166–173.
Marian, J., Cai, W., Bulatov, V.V., 2004. Dynamic transition from smooth to rough to twinning in dislocation motion. Nat. Mater. 3, 158–163.
Mayer, A.E., et al., 2013. Modeling of plasticity and fracture of metals at shock loading. J. Appl. Phys. 113, 193508.
edited byMeyers, M.A., et al., 2009. Dislocation in shock compression and release. In: J.P. Hirth, Kubin, L. (Eds.), Dislocations in Solids, edited by.
Molodets, A.M., 2005. Shock compression of preheated molybdenum. High Press. Res. 35, 211–216.
Ojha, A., Sehitolu, H., 2014. Twinning stress prediction in BCC metals and alloys. Philos. Mag. Lett. 94 (10), 647–657.
Pang, B., et al., 2018. The defect evolution in shock loaded tantalum single crystals. Acta Mater. 148, 482–491.
Po, G. et al., 2016, A phenomenological dislocation mobility law for BCC metals, Acta Mater., 119, 123–135.
Roters, F., et al., 2010. Overview of constitutive laws, kinematics, homogenization and multiscale methods in crystal plasticity finite-element modeling: theory, experiments, applications. Acta Mater. 58, 1152–1211.
Smirnov, B.I., 1967. Temperature dependence of the Peierls-Nabarro forces in body-centered cubic metals. Mech. Mater. 3, 498–499.
Soga, N., 1966. Comparison of measured and predicted bulk moduli of tantalum and tungsten at high temperatures. J. Appl. Phys. 37, 3416–3420.
Varshi, Y.P., 1970. Temperature dependence of the elastic constants. Phys. Rev. B 2, 3952–3958.
Voyiadjis, G.Z., Abed, F.H., 2005. A physically based constitutive model for fcc metals with applications to dynamic hardness. Mech. Mater. 37, 549–563.
Walker, E., 1978. Anomalous temperature behavior of the shear elastic constant C_{44} in vanadium. Solid State Commun. 28, 587–589.
Walker, E., Bujard, P., 1980. Anomalous temperature behavior of the shear elastic constant C_{44} in tantalum. Solid State Commun. 34, 691–693.
Wu, P.D., et al., 2015. A constitutive model of twin nucleation, propagation and growth in magnesium crystals. Mater. Sci. Eng. A 625, 140–145.
Zaretsky, E.B., 2009. Shock response of iron between 143 and 1275 K. J. Appl. Phys. 106, 023510.
Zaretsky, E.B., Kanel, G.I., 2014. Tantalum and vanadium response to shock wave loading at normal and elevated temperatures. Non-monotonous decay of the elastic wave in vanadium. J. Appl. Phys. 115, 243502.
Zaretsky, E.B., Kanel, G.I., 2015. Yield stress, polymorphic transformation, and spall fracture of shock- loaded iron in various structural states and at various temperatures. J. Appl. Phys. 117, 195901.
Zaretsky, E.B., Kanel, G.I., 2016. Invariability of rate dependences of normalized flow stress in niobium and molybdenum under conditions of shock compression. J. Appl. Phys. 120, 105901.
Zaretsky, E.B., Kanel, G.I., 2017. The high temperature impact response of tungsten and chromium. J. Appl. Phys. 122, 115901.